

Measuring the mass distribution of voids with stacked weak lensing

Yuichi Higuchi^{1*}, Masamune Oguri² and Takashi Hamana³

¹*Department of Astronomy, Graduate school of Science, University of Tokyo, Tokyo 113-0033, Japan*

²*Kavli Institute for the Physics and Mathematics of the Universe (Kavli IPMU, WPI), University of Tokyo, Chiba 277-8583, Japan*

³*National Astronomical Observatory of Japan, Mitaka, Tokyo 181-8588, Japan*

6 August 2021

ABSTRACT

We study the prospects for measuring the dark matter distribution of voids with stacked weak lensing. We select voids from a large set of N -body simulations, and explore their lensing signals with the full ray-tracing simulations including the effect of the large-scale structure along the line-of-sight. The lensing signals are compared with simple void model predictions to infer the three-dimensional mass distribution of voids. We show that the stacked weak lensing signals are detected at significant level ($S/N \geq 5$) for a 5000 degree² survey area, for a wide range of void radii up to ~ 50 Mpc. The error from the galaxy shape noise little affects lensing signals at large scale. It is also found that dense ridges around voids have a great impact on the weak lensing signals, suggesting that proper modeling of the void density profile including surrounding ridges is essential for extracting the average total underdens mass of voids.

Key words: gravitational lensing: weak, stacked lensing, large-scale structure of universe

\LaTeX – style files: mn2e.sty

1 INTRODUCTION

Cosmological structure formation and matter distribution of the universe depend on models of cosmology. Therefore one of the keys for constraining cosmology is to understand the distribution of matter. High density peaks in the matter density distribution which correspond to galaxies and galaxy clusters have been well studied (Broadhurst et al. 2005; Umetsu et al. 2011; Oguri et al. 2012). These overdensity regions are used for constraining cosmology (Takada 2006; Oguri & Takada 2011; Prada et al. 2012). On the other hand, negative density troughs which correspond to voids have attracted less attention in spite of its long history (Kirshner et al. 1981) and the fact that they fill more than 80% of the volume of the universe and therefore are an essential component of large scale structure (LSS) of the universe.

There has been analytical work that studied the formation and evolution of voids (Fillmore & Goldreich 1984; Suto et al. 1984; Furlanetto & Piran 2006). The early evolution of void is well described by a spherical collapse model. In this model underdense regions expand and gradually become deep until the shell crossing occurs (Peebles 1980). Effects of different cosmology on voids have also

been studied (Moffat 2006; Park & Lee 2007; Lee & Park 2009; Kamionkowski et al. 2009; Li et al. 2012). These papers pointed out possibilities for constraining cosmology with voids, including primordial non-gaussianity and modified gravity theories.

On the other hand, observationally various void finding algorithms have been applied to redshift surveys such as the Sloan Digital Sky Survey (SDSS) to study properties of voids (Strauss et al. 1992; Jones et al. 2004; Colberg et al. 2008; Pan et al. 2012). It was found that voids are significantly underdense in their observations which use galaxy distribution for locating voids. These results are broadly consistent with theoretical predictions. However many problems still exist when comparing simulations with observations (e.g. Ryden & Turner 1984; Klypin et al. 1999; Tavasoli et al. 2012). For example, the matter distribution of voids is estimated by assuming the galaxy bias, and therefore the uncertainty of the bias is one of the most serious challenges in void studies.

By contrast, gravitational lensing traces all matters regardless of baryon or dark matter. In fact, the possibility of studying voids with weak gravitational lensing was discussed in Jain & Van Waerbeke (2000), and a possible statistical detection was reported by Miyazaki et al. (2002). While lensing signals of individual voids are weak (Amendola et al. 1999), stacked weak lensing technique may enable to detect

* E-mail: yuichi.higuchi@nao.ac.jp

such signals and allows us to study the true matter distribution in voids without any assumptions on the galaxy bias. This is exactly what we explore in this paper with paying a special attention to its prospect with next generation wide field surveys such as Subaru Hyper Suprime-cam survey (HSC) (Miyazaki et al. 2006).

This paper is organized as follows. In Sec.2, we describe basics of our analyzing techniques, focusing on how we can obtain information of dark matter distribution from gravitational lensing. In Sec.3, we describe our simulation and void finding algorithm. In Sec.4, we describe the mass function of voids. The void model used for fitting lensing signals is presented in Sec.5. In Sec.6, we show the result of the stacking analysis and fitting with our model. We summarize our results in Sec.7.

2 BASICS OF ANALYSIS

2.1 basics of gravitational lensing

Throughout this paper, we assume a spatially flat universe. Gravitational lensing effects on the α - β plane are characterized by an isotropic stretching called convergence $\kappa(\theta)$ and anisotropic distortion called shear $\gamma_1(\theta)$ and $\gamma_2(\theta)$. They are related to the two dimensional analogue of the Newtonian gravitational potential $\psi(\theta)$ as

$$\kappa(\theta) = \frac{1}{2} \nabla^2 \psi(\theta), \quad (1)$$

$$\gamma_1(\theta) = \frac{1}{2} \left(\frac{\partial^2 \psi(\theta)}{\partial \theta_\alpha^2} - \frac{\partial^2 \psi(\theta)}{\partial \theta_\beta^2} \right), \quad (2)$$

$$\gamma_2(\theta) = \frac{\partial^2 \psi(\theta)}{\partial \theta_\alpha \partial \theta_\beta}, \quad (3)$$

Then convergence at an angular position θ is represented as

$$\kappa(\theta) = \frac{3H_0^2 \Omega_{m0}}{2c^2} \frac{D_{ls} D_l}{D_s a_1^3} \int dz \delta(\theta, z), \quad (4)$$

where z is the line-of-sight distance (fig.1), $\delta(\theta, z)$ is density contrast defined by

$$\delta(\theta, z) = \frac{\rho(\theta, z) - \bar{\rho}(z)}{\bar{\rho}(z)}, \quad (5)$$

with $\bar{\rho}(z)$ being the average density at z . H_0 and Ω_{m0} are hubble parameter and matter density parameter at present, respectively, and a_1 is scale factor at the lens position. D_s , D_l and D_{ls} are angular diameter distance which are expressed as

$$D_s = a_s \chi_s, D_l = a_l \chi_l, D_{ls} = a_s (\chi_s - \chi_l), \quad (6)$$

where a_s is the scale factor at a source position. χ_s, χ_l are comoving distance from an observer to source and lens.

It is useful to introduce the tangential distortion component γ_+ with respect to a certain point, and the cross component γ_\times which is rotated by 45° . The tangential shear components include all information of lens, if a lensing mass profile is axisymmetric on the sky. These two components are defined with γ_1 and γ_2 as

$$\begin{pmatrix} \gamma_+ \\ \gamma_\times \end{pmatrix} = \begin{pmatrix} -\cos 2\eta & -\sin 2\eta \\ -\sin 2\eta & \cos 2\eta \end{pmatrix} \begin{pmatrix} \gamma_1 \\ \gamma_2 \end{pmatrix}, \quad (7)$$

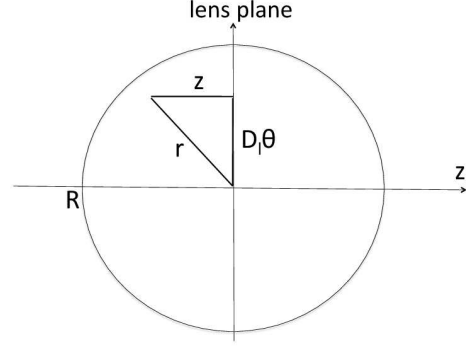


Figure 1. Definition of the coordinate system

where η is the angle between axis- α and θ . The sign of tangential shear is chosen so that a background galaxy shape becomes tangentially deformed for positive and radially deformed for negative with respect to the lens center.

Weak lensing signal is so small that it is difficult to measure masses down to low mass objects. However, by stacking lensing signals from many samples, we can reduce errors which limit to obtain information on the objects (e.g. Mandelbaum et al. 2006; Okabe et al. 2010; Oguri et al. 2012). Therefore stacked lensing is a powerful tool for measuring average dark matter distributions of targets. The stacked lensing technique is also used to constrain cosmological parameters (e.g. Oguri & Takada 2011; Rozo et al. 2010). In the weak lensing limit, the average tangential shear profile at θ_i is related to the convergence (Bartelmann & Schneider 2001) as

$$\langle \gamma_+ \rangle(\theta_i) = \bar{\kappa}(\theta < \theta_i) - \langle \kappa \rangle(\theta_i), \quad (8)$$

where $\langle \dots \rangle$ denotes average value in the circular annulus, the first term is the mean convergence within a circular aperture of radius θ_i defined as

$$\bar{\kappa}(\theta < \theta_i) = \frac{1}{\pi \theta_i^2} \int_{\theta \leq \theta_i} d\theta' \kappa(\theta'), \quad (9)$$

and the second term is the mean convergence in the i -th radial bin. The average cross shear component $\langle \gamma_\times \rangle(\theta < \theta_i)$ must be zero in weak lensing caused by the standard scalar gravitational potential.

In stacked lensing method, the following statistical uncertainties on tangential shear should be considered

$$\sigma_{\gamma_+}^2 = \sigma_{\text{void}}^2 + \sigma_{\text{LSS}}^2 + \sigma_{\text{shape}}^2, \quad (10)$$

where σ_{void}^2 is the statistical error coming from deference in the structure of each void used in stacking analysis, σ_{LSS}^2 is the error coming from large-scale structure along the line-of-sight, and σ_{shape}^2 is the shape noise error coming from the intrinsic ellipticity of galaxies used for weak lensing measurements. Considering errors coming from structure of voids and LSS, the covariance matrix between i -th and j -th radial bin is estimated as

$$\sigma_{\gamma_+(\theta_i, \theta_j)}^2 = \frac{\sum_l^{N_v} (\gamma_{+,l}(\theta_i) - \langle \gamma_+(\theta_i) \rangle) (\gamma_{+,l}(\theta_j) - \langle \gamma_+(\theta_j) \rangle)}{N_v}, \quad (11)$$

where $\gamma_{+,l}(\theta_i)$ is the tangential shear in the l -th void at i -th radial bin and N_v is the number of voids. In addition to this, the error from intrinsic ellipticity shown in Van Waerbeke et al. (2000) is determined as

$$\sigma_{\text{shape}}^2 = \frac{\sigma_\epsilon^2}{N_v n_g S}, \quad (12)$$

where σ_ϵ is the rms amplitude of the intrinsic ellipticity distribution, n_g is the number density of galaxies and S is the area of a bin. Throughout this paper we adopt $\sigma_\epsilon = 0.4$ and $n_g = 30 \text{ arcmin}^{-2}$. As we shall show in below, shape noise becomes the dominant error at only small scale, on the other hand the other errors becomes dominant at large scale (sec.6.5). We ignore other observational systematics such as imperfections in the telescope and electric devices of detectors.

2.2 Signal to noise ratio of stacked lensing

A useful way to quantify the observability is to calculate the total Signal-to-Noise (S/N) ratio over the considered scale. We follow the definition by Oguri & Takada (2011). The total S/N is expressed as

$$\left(\frac{S}{N}\right)^2 = \sum_{ij} \gamma_+(\theta_i) [\text{cov}(\gamma_+(\theta_i), \gamma_+(\theta_j))]^{-1} \gamma_+(\theta_j), \quad (13)$$

where the summation indices i, j run over radial bins. We evaluate the S/N with covariance matrix with and without the shape noise component to see the effect of the shape noise. The S/N is related to the accuracy of the mass estimate. More specifically, they are related as (Oguri & Takada 2011)

$$\frac{\Delta M}{M} \sim \left(\frac{S}{N}\right)^{-1} \left(\frac{d \ln \gamma_+}{d \ln M}\right)^{-1}. \quad (14)$$

Therefore S/N is proportional to the accuracy for constraining the mass of the object.

2.3 Mass reconstruction

It is sometimes useful to derive a model independent information of the mass from weak lensing data (e.g. Okabe et al. 2010; Squires et al. 1996 and Squires et al. 1997). Convergence in each circular annulus of radius θ is related to the projected mass density

$$\kappa(\theta) = \frac{\Sigma(\theta)}{\Sigma_{\text{cr}}}, \quad (15)$$

where Σ_{cr} is critical projected mass density defined as

$$\Sigma_{\text{cr}} = \frac{c^2}{4\pi G} \frac{D_s}{D_l D_{ls}}. \quad (16)$$

The mass is related to convergence (Bartelmann & Schneider 2001) as

$$M(< \theta) = \Sigma_{\text{cr}} D_l^2 \int d\theta'^2 \kappa(\theta') U(\theta' - \theta), \quad (17)$$

where $U(\theta)$ is weight function which we adopt $U(\theta) = 1$ in our calculation. When we estimate void masses which are removed from underdensity regions, we calculate those only for the region with $\kappa(\theta) < 0$. For the reconstruction from

tangential shear, more careful calculation called ζ -statistics (Fahlman et al. 1994; Clowe et al. 2000) is needed.

Furthermore the mass is related to the average mass density $\bar{\rho}$ and void radius R

$$\begin{aligned} M &= \left| \frac{4}{3} \pi R^3 \bar{\rho} - \frac{4}{3} \pi R^3 \rho \right| \\ &= \left| \frac{4}{3} \pi R^3 (\bar{\rho} - \rho) \right| \\ &= \frac{4}{3} \pi R^3 \bar{\rho} |\delta|, \end{aligned} \quad (18)$$

where we assume the mass density ρ is constant in the region.

3 SIMULATION

3.1 Ray-tracing simulation

We use a large set of ray-tracing simulation which are carried out in Sato et al. (2009). To carry out N -body simulation, they use the parallel Tree-Particle Mesh code Gadget-2 (Springel 2005 and see Sato et al. 2009 for simulation details). The simulation employ 256^3 particles in a cubic box of $240h^{-1}$ Mpc on a side. Cosmological parameters are assumed as hubble parameter $H_0 = 73.2 \text{ km/s/Mpc}$, matter density $\Omega_m = 0.238$, baryon density $\Omega_b = 0.042$, dark energy density $\Omega_\Lambda = 0.762$, equation of state parameter $w = -1$, spectral index $n_s = 0.958$ and variance of density fluctuation with $8 h^{-1}$ Mpc $\sigma_8 = 0.76$. These cosmological parameters follows WMAP 3-year results (Spergel et al. 2007). By using results of N -body simulation, they carry out ray-tracing simulation with the algorithm described in Hamana & Mellier (2001). We refer the reader to the above reference for more details. We use 200 realizations with a fixed source redshift of $z_s \simeq 1.0$. The area of each realization is 5×5 degree². Therefore the effective total area is 5000 degree².

3.2 Void Finder

To search for voids in the simulation data, we employ the public code Void Finder (Foster & Nelson 2009), which is based on the void finding algorithm developed by Hoyle & Vogeley (2004) and Hoyle et al. (2005). We refer the reader to the above references for full details of the algorithm and its implementation. Here we describe only points which are specific to this study.

In this study, we use dark matter haloes for tracers of underlying dark matter distribution. The dark matter haloes are identified in the N -body simulations using friend-of-friend (FOF) algorithm with the linking length of $b = 0.2$ (Oguri & Hamana 2012). The Void Finder is applied to haloes with masses larger than $2.2 \times 10^{12} M_\odot$. The Void Finder includes some parameters for which we adopt the same parameters recommended in Foster & Nelson (2009), except for the voids minimum radius parameter ξ . We take two values for the minimum radius, $\xi = 5$ and 10 Mpc, to see the effect of its choice on void finding. For stacked lensing analysis, we use voids with the radii (which is defined in the Void Finder) between $R = 15$ and 45 Mpc and in the redshift range $0.4 \leq z \leq 0.6$ because lensing efficiency is expected to be high in the redshift range. The number of haloes within the redshift range is 2.5×10^6 . For comparison, we also use voids

with $15 \leq R \leq 40$ Mpc in the redshift range of $0.1 \leq z \leq 0.3$. The number of halos used in this redshift range is 6.0×10^5 .

4 PRESS-SCHECHTER THEORY

We use the modified Press-Schechter (PS) formalism (see e.g. Kamionkowski et al. 2009) for predicting number counts of voids analytically.

In the standard PS theory (Press & Schechter 1974), regions which exceed the spherical collapse linear overdensity $\delta_c = 1.689$ are considered to end up a halo. The probability that a given point lies in a region with the linear density fluctuation $\delta > \delta_c$ is

$$P(\delta > \delta_c | M) = \frac{1}{\sqrt{2\pi}} \frac{\sigma(R)}{\delta_c} \exp\left(-\frac{\delta_c^2}{2\sigma^2(R)}\right), \quad (19)$$

where M is a halo mass defined with a radius R as,

$$M = \frac{4\pi}{3} \bar{\rho} R^3, \quad (20)$$

and $\sigma^2(R)$ is the rms density fluctuation defined as,

$$\sigma^2(R) = \int \frac{dk k^2}{2\pi^2} W^2(kR) P(k), \quad (21)$$

where $W(kR)$ is the Fourier transform of the window function and $P(k)$ is the matter power spectrum. Therefore the mass function $n(M)$ is reduced as

$$\begin{aligned} n(M) dM &= 2\bar{\rho} [P(\delta > \delta_c | M) - P(\delta > \delta_c | M + dM)] \\ &= \sqrt{\frac{2}{\pi}} \frac{\bar{\rho}}{M^2} \left| \frac{d \ln \sigma(R)}{d \ln M} \right| \frac{\delta_c}{\sigma(R)} \exp\left(-\frac{\delta_c^2}{2\sigma^2(R)}\right) dM. \end{aligned} \quad (22)$$

In order to estimate the number count of voids based on the modified PS theory, we replace δ_c in eq.22 to linear underdensity $|\delta_v|$.

In our calculation, gaussian window function and the CDM transfer function by BBKS (Bardeen et al. 1986) are used. For estimating the number count at a given redshift, the rms linear density fluctuation $\sigma(R)$ is evolved by using the linear growth factor.

5 VOID MODEL

Density profiles of voids have been studied in previous works (e.g. Sheth & van de Weygaert 2004; Pan et al. 2012), which indicate that the matter density is almost constant over the underdense region and there is a very sharp spike called a ridge at the edge of voids.

In order to make a simple void model which includes the properties found in the previous work, we consider a spherically symmetric void model including ridges, which we call a double top-hat model (fig.2). In this model, we set mass density $\rho(r)$ as

$$\rho(r) = \begin{cases} \rho_1 & (r \leq R_1), \\ \rho_2 & (R_1 < r \leq R_2), \\ 0 & (R_2 < r), \end{cases} \quad (23)$$

where r is the distance from a void center (fig.1), ρ_1 and ρ_2 are constant in each region. We assume that the total mass

between the void region and the ridge region should be compensated each other. Thus the masses between two regions are related as

$$\frac{4}{3} \pi R_1^3 (\bar{\rho} - \rho_1) = \frac{4}{3} \pi (R_2^3 - R_1^3) (\rho_2 - \bar{\rho}). \quad (24)$$

From eq.24, ρ_2 is expressed with ρ_1 , R_1 and R_2

$$\rho_2 = \bar{\rho} + \frac{1}{1 - (R_2/R_1)^3} (\rho_1 - \bar{\rho}). \quad (25)$$

From eq.23 and eq.25, density contrast is reduced as

$$\delta(r) = \begin{cases} \delta & (r < R_1), \\ \frac{\delta}{1 - (R_2/R_1)^3} & (R_1 < r < R_2), \\ 0 & (r > R_2). \end{cases} \quad (26)$$

An advantage of this double top-hat model is that its lensing properties can be computed analytically. By using eq.4 and eq.26, convergence is calculated as

$$\begin{aligned} \kappa(\theta) &= \frac{3H_0^2 \Omega_{m0}}{2c^2} \frac{D_{ls} D_l}{D_s a_l^3} \int_{-D_l \sqrt{\theta_2^2 - \theta^2}}^{D_l \sqrt{\theta_2^2 - \theta^2}} dz \left\{ \delta \Theta(R_1 - r) \right. \\ &\quad \left. + \frac{\delta}{1 - (R_2/R_1)^3} \Theta(r - R_1) \Theta(R_2 - r) \right\} \\ &= \frac{3H_0^2 \Omega_{m0}}{2c^2} \frac{D_{ls} D_l}{D_s a_l^3} \cdot 2\delta D_l \cdot \\ &\quad \left[\left\{ \frac{\sqrt{\theta_2^2 - \theta^2} - \sqrt{\theta_1^2 - \theta^2}}{1 - (\theta_2/\theta_1)^3} + \sqrt{\theta_1^2 - \theta^2} \right\} \Theta(\theta_1 - \theta) \right. \\ &\quad \left. + \left\{ \frac{\sqrt{\theta_2^2 - \theta^2}}{1 - (\theta_2/\theta_1)^3} \right\} \Theta(\theta - \theta_1) \Theta(\theta_2 - \theta) \right], \end{aligned} \quad (27)$$

where $\Theta(r)$ is a step function. The radii are related to angles

$$r = D_l \theta, \quad (28)$$

$$R_i = D_l \theta_i, \quad (29)$$

where the induce i takes 1 or 2.

In addition to the analytical expression of convergence, we can also calculate the tangential shear analytically. From eq.8, the tangential shear reduces to

$$\begin{aligned} \langle \gamma_+ \rangle(\theta) &= \bar{\kappa}(< \theta) - \langle \kappa \rangle(\theta) \\ &= \frac{2}{\theta^2} \int_0^\theta d\theta' \theta' \kappa(\theta') - \langle \kappa \rangle(\theta). \end{aligned} \quad (30)$$

From eq.27, the integration becomes

$$\begin{aligned} \int_0^\theta d\theta' \theta' \kappa(\theta') &= \\ &\quad \left\{ \frac{A}{3} \frac{(\theta_2/\theta_1)^3 (\theta_1^2 - \theta^2)^{\frac{3}{2}} - (\theta_2^2 - \theta^2)^{\frac{3}{2}}}{1 - (\theta_2/\theta_1)^3} \right\} \Theta(\theta_1 - \theta) \\ &\quad - \left\{ \frac{A}{3} \frac{(\theta_2^2 - \theta^2)^{\frac{3}{2}}}{1 - (\theta_2/\theta_1)^3} \right\} \Theta(\theta - \theta_1) \Theta(\theta_2 - \theta), \end{aligned} \quad (31)$$

where $A = \frac{3H_0^2 \Omega_{m0}}{c^2} \frac{D_{ls} D_l^2}{D_s a_l^3} \delta$. Therefore with eq.27 and eq.31,

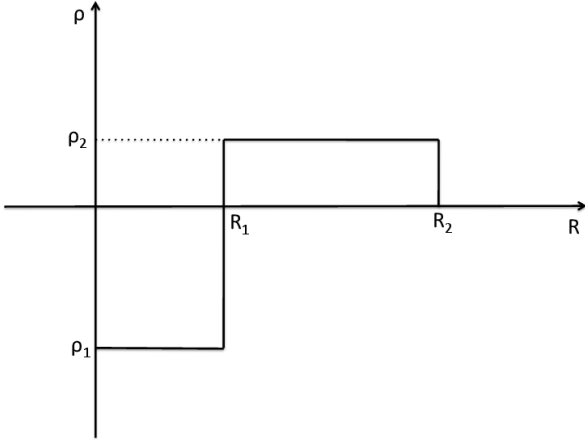


Figure 2. Double top-hat void model. In $r < R_1$, $\rho(r)$ is equal to constant ρ_1 , and $R_1 < R < R_2$, $\rho(r)$ is equal to constant ρ_2 . Relative amplitudes between ρ_1 and ρ_2 are determined by the requirement of the mass compensation. ρ is zero outside R_2 .

an analytical expression of the tangential shear is derived as

$$\begin{aligned} \langle \gamma_+ \rangle(\theta) = & \left[\frac{A}{3\theta^2} \frac{1}{1 - (\theta_2/\theta_1)^3} \left\{ (\theta_2/\theta_1)^3 (2\theta_1^2 + \theta^2) \sqrt{\theta_1^2 - \theta^2} \right. \right. \\ & \left. \left. - (2\theta_2^2 + \theta^2) \sqrt{\theta_2^2 - \theta^2} \right\} \right] \Theta(\theta_1 - \theta) \\ & - \left[\frac{A}{3\theta^2} \frac{(2\theta_2^2 + \theta^2) \sqrt{\theta_2^2 - \theta^2}}{1 - (\theta_2/\theta_1)^3} \right] \Theta(\theta - \theta_1) \Theta(\theta_2 - \theta). \quad (32) \end{aligned}$$

We assume the density contrast is equal to zero outside the second top-hat. Therefore the convergence and the tangential shear must be zero in that region.

Model parameters are determined by the standard χ^2 minimization method with simulation results. We define the estimator χ^2 as

$$\begin{aligned} \chi^2 = & \sum_{i,j} (\gamma_{+,model}(\theta_i) - \gamma_{+,sim}(\theta_i)) \\ & \times \left[\text{cov}(\gamma_{+,sim}(\theta_i), \gamma_{+,sim}(\theta_j)) \right]^{-1} \\ & \times (\gamma_{+,model}(\theta_j) - \gamma_{+,sim}(\theta_j)), \quad (33) \end{aligned}$$

where $\gamma_{+,model}(\theta_i)$ and $\gamma_{+,sim}(\theta_i)$ are tangential shear in the model and simulation at i -th radial bin.

6 RESULT

6.1 Number counts of voids

In order to check effects of the minimum radius parameter ζ in the Void Finder on void finding, we run the Void Finder with both $\zeta = 5$ Mpc and $\zeta = 10$ Mpc. We compute the void number counts as a function of void radius for the two cases, and present the results in Figure.3, where voids in the redshift range $0 \leq z \leq 1$ are considered. The figure clearly shows that the number counts depend on the choice of the minimum radius. It is found that the number counts of voids

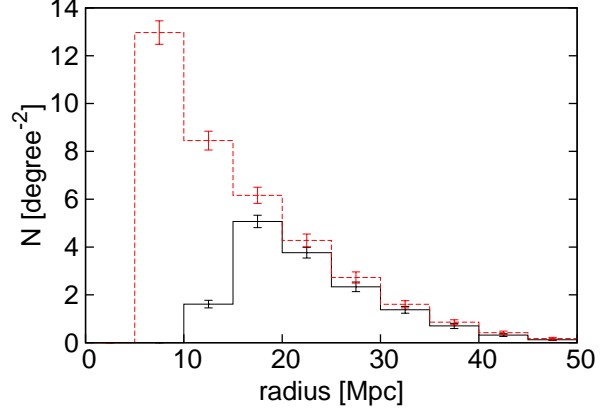


Figure 3. Number counts of voids in the simulation for the redshift range $0 \leq z \leq 1$. x-axis is void radius. y-axis is number counts of void in each bin. The dashed and solid line histograms show the number counts with minimum radius $\zeta = 5$ Mpc and $\zeta = 10$ Mpc. Error bar shows 1σ with 200 realizations.

for the larger minimum radius case is smaller than the other case with two features; one is the cutoff at smaller scales and the other is the effect originated from the void finding algorithm. The reason of the former is a natural consequence of the large minimum radius of $\zeta = 10$ Mpc, which prevents to identify voids with the size smaller than that. For the latter, the same trend is found in Foster & Nelson (2009). As is found in Fig 3, these effects are not significant for larger radii $R \geq 20$ Mpc. It should be also noted that not all the voids are associated with *legitimate* cosmological voids but some are *spurious* voids originated from a lack of halos for those regions to which the Void Finder is adopted. The spurious voids are likely mis-identified when a void radius is similar to or smaller than the mean separation of halos. In our case, the mean separation of halos is about 7 Mpc, thus voids with a radius ≥ 15 Mpc might not be seriously affected by this effect regardless of the choice of the minimum radius. Taking the above points into account, in the following stacking analysis, we take the minimum radius $\zeta = 5$ Mpc, and consider voids with the radius ≥ 15 Mpc.

6.2 Direct estimation of void masses

In order to estimate mass profiles and void masses, we stack lensing signals from voids selected by the Void Finder. We estimate the mass in each void sample from the result of stacking and eq.17.

We divide voids located by Void Finder into 6 groups based on the void radius determined by the Void Finder. Here we select only voids that are located in the redshift range $0.4 \leq z \leq 0.6$. We align the centers of voids determined by the Void Finder and stack those in each group. The radii and number of voids used for stacking analysis are showed in table.1. Points with errors in figure.4 and figure.5 show stacked convergence and tangential shear profiles in each radius.

The void masses we estimate from the convergence profiles with eq.17 are presented in table.1. The calculation is carried out only for the region $\kappa(\theta) < 0$. We find that void masses that are directly estimated from the convergence profiles are comparable to typical cluster masses ($\sim 10^{14} M_\odot$). As

Table 1. Details of stacking. Column (1): radius of voids determined by the void finder; Column(2): the number count of voids in the each radial bin and the redshift range $z_1 = 0.4 \sim 0.6$; Column(3): void mass calculated by integrating the $\kappa(\theta) < 0$ region.

Radius [Mpc]	Number of voids	Mass from $\kappa(\theta) < 0$ [M_\odot]
15 ~ 20	5246	9.03×10^{13}
20 ~ 25	3892	4.45×10^{14}
25 ~ 30	2446	1.81×10^{15}
30 ~ 35	1400	3.06×10^{15}
35 ~ 40	724	4.01×10^{15}
40 ~ 45	320	3.26×10^{15}

we will see below, these void masses are smaller than ones estimated from the double top-hat model because of the effect of surrounding ridges.

6.3 Fitting the convergence profile

In order to compute convergence and tangential shear profiles of voids analytically, we assume the double top-hat model presented in sec.5. We consider the source at $z_s = 1.0$ and the lens at $z_1 = 0.5$. For our model, we treat δ , θ_1 and θ_2 in eq.27 and eq.32 as free parameters to fit stacked lensing signals in our simulation. At first, we ignore shape noise and only consider noises from LSS and structures of voids in the process of fitting. Fitting is performed in the parameter range $-1 \leq \delta \leq 0$, $0' \leq \theta_1 \leq 100'$, $0' \leq \theta_2 \leq 300'$. We sum up χ^2 over the radius range $0' \leq \theta \leq 90'$ for $15 \leq R \leq 30$ Mpc, and $0' \leq \theta \leq 180'$ for $30 \leq R \leq 45$ Mpc.

Fig.4 compares the convergence profiles from the simulation with the model. Model fitting is carried out for convergence profiles. We find that our simple model reproduces lensing signals in simulation well. Best-fit parameters used in this plot are summarized in table.2. Using these parameters, we estimate total void masses, i.e. the total mass removed from the void region (table.2). Our model fits both convergence and tangential shear profile well, except for the case with $15 \leq R \leq 20$ Mpc. There are two reasons why fitting fails for this case. The first is a problem in the Void Finder. As we and Foster & Nelson (2009) showed, the number counts of voids depend on the minimum radius parameter ζ of Void Finder especially for smaller radii, indicating that the Void Finder mis-identifies spurious voids. The second reason is that the double top-hat model with the requirement of the mass compensation may not be very realistic.

Total void masses calculated by fitting the convergence profile with our model are a few times larger than masses estimated from direct integration at $\kappa(\theta) < 0$. This is because observed convergence value is cumulative value from sources to an observer. Therefore when we calculate mass we should consider the effect from the ridge outside the void. Otherwise we underestimate total void mass. Also, the size of underdense regions $D_l\theta_1$ determined by model fitting are found to be smaller than radii defined in the Void Finder. This is probably because the halo catalogue we use for void finding does not exactly trace the underlying matter distribution.

6.4 Fitting the tangential shear profile

We also use tangential shear profile for finding best-fit parameters. We set same condition for searching best-fit parameters as that used for fitting the convergence profiles.

Figure.5 summarizes tangential shear profiles in the simulation and best-fit models. Table.3 shows best-fit parameters and total void masses determined from the fitting. Total void masses are estimated with eq.18 as we have done in sec.6.3. We find that the best-fit parameters and the resulting total void masses are very similar to those obtained from fitting convergence profiles (table.2), suggesting the consistency of our analysis.

6.5 Signal-to-Noise ratio

Using the stacked lensing covariance matrix we derived, we estimate S/N defined in eq.13 for cases with and without the shape noise.

Fig.6 shows tangential shear profiles with error bars with and without the shape noise considered. For illustrative purpose, points are shifted by 2 arcmin. Stacking analysis are carried out for voids in the radial range $20 \leq R \leq 25$ Mpc and the redshift range $0.4 \leq z_1 \leq 0.6$. The shape noise is estimated from eq.12. The error from the shape noise is added to the diagonal elements of the covariance matrix. The effect from the shape noise becomes a dominant component of the error at small scale, because the number of galaxies in each radial annulus is proportional to the radius under the condition that radial bin size Δr is constant. On larger scales, the shape noise is not a dominant component of the error.

Total S/N is estimated for voids in the redshift ranges $0.4 \leq z_1 \leq 0.6$ and $0.1 \leq z_1 \leq 0.3$ by using eq.13. Table.4 shows S/N with and without the shape noise for each radius. Table.5 shows S/N for the redshift range $0.1 \leq z_1 \leq 0.3$. Table.4 and table.5 show that the stacked lensing signals are detected at significant level of $S/N \geq 5$. Adding the shape noise degrades S/N, but the effect is relatively minor. Compared with total S/N in the redshift range $0.4 \leq z_1 \leq 0.6$, total S/N in the redshift range $0.1 \leq z_1 \leq 0.3$ are degraded. The error coming from the diversity in the structure of each void increases because the number of voids decreases as the redshift range becomes low. However, S/N for individual void in the redshift range $0.1 \leq z_1 \leq 0.3$ is higher than that in the redshift range $0.4 \leq z_1 \leq 0.6$ because of the larger apparent sizes of voids at lower redshift.

6.6 Comparison of the mass function of voids

Here we derive the void mass function and fit it with the modified PS model (sec.4). We consider voids in the redshift range of $0.4 \leq z \leq 0.6$. The number counts of voids as a function of the void radius are derived in sec. 6.1. Thus, we have the void ‘‘radius’’ function. In order to transform it to the ‘‘mass’’ function (namely, transforming $n(R)$ to $n(M)$), we take the following approach; The void masses for each radius group are evaluated from the tangential shear profiles with the double top-hat model (sec.6.4). We assume the following relationship between the void radius and mass;

$$M = A_0 R^3, \quad (34)$$

Table 2. Best fit parameters and derived total void mass. These parameters are determined from convergence profiles. Column (1): radius of void determined with the void finder; Column (2): density contrast; Column (3): radius of underdense region; Column (4): radius of overdense region; Column (5): void mass derived from the double top-hat model

Radius in the void finder [Mpc]	δ	$D_1\theta_1$ [Mpc]	$D_1\theta_2$ [Mpc]	Void mass [M_\odot]
15 ~ 20	-0.390	12.1	25.5	1.46×10^{15}
20 ~ 25	-0.194	19.1	27.5	2.83×10^{15}
25 ~ 30	-0.244	21.0	63.0	4.78×10^{15}
30 ~ 35	-0.424	16.6	109	4.09×10^{15}
35 ~ 40	-0.316	25.5	59.8	1.10×10^{16}
40 ~ 45	-0.220	27.3	38.9	2.73×10^{16}

Table 3. Best-fit parameters and derived total void mass. These parameters are determined from tangential shear profiles. Column (1): radius of void determined with the void finder; Column (2): density contrast; Column (3): radius of underdense region; Column (4): radius of overdense region; Column (5): void mass derived from the double top-hat model

Radius in the void finder [Mpc]	δ	$D_1\theta_1$ [Mpc]	$D_1\theta_2$ [Mpc]	Void mass [M_\odot]
15 ~ 20	-0.398	12.2	25.3	1.53×10^{15}
20 ~ 25	-0.170	19.1	27.6	2.50×10^{15}
25 ~ 30	-0.250	19.0	109	3.63×10^{15}
30 ~ 35	-0.403	16.8	40.0	4.00×10^{15}
35 ~ 40	-0.290	25.5	59.8	1.01×10^{16}
40 ~ 45	-0.183	27.3	39.5	7.80×10^{15}

Table 4. Signal-to-noise ratio, integrated over angular scales considered in the redshift range $z = 0.4 \sim 0.6$. Column (1): radius of void determined with the void finder; Column (2): the number count of voids in the each radial bin and the redshift range $z = 0.4 \sim 0.6$; Column (3): S/N derived from tangential shear without the shape noise; Column (4): S/N derived from tangential shear with the shape noise; Column (5): S/N for one void. It is estimated from information of tangential shear with shape noise and the number of voids (table.1)

Radius [Mpc]	Number of voids	S/N (tangential shear w/o shape noise)	S/N (tangential shear w/ shape noise)	$(S/N)/\sqrt{N_{void}}$ (w/ shape noise)
15 ~ 20	5246	11.0	9.18	0.127
20 ~ 25	3892	8.25	6.97	0.112
25 ~ 30	2446	7.55	6.51	0.132
30 ~ 35	1400	8.19	6.76	0.181
35 ~ 40	724	7.57	6.25	0.232
40 ~ 45	320	7.89	5.39	0.301

Table 5. Signal-to-noise ratio, integrated over angular scales considered in the redshift range $z = 0.1 \sim 0.3$. Column (1): radius of void determined with the void finder; Column (2): the number count of voids in the each radial bin and the redshift range $z = 0.1 \sim 0.3$; Column (3): S/N derived from tangential shear without the shape noise; Column (4): S/N derived from tangential shear with the shape noise; Column (5): S/N for one void

Radius [Mpc]	Number of voids	S/N (tangential shear w/o shape noise)	S/N (tangential shear w/ shape noise)	$(S/N)/\sqrt{N_{void}}$ (w/ shape noise)
15 ~ 20	1798	6.89	6.09	0.144
20 ~ 25	1097	5.69	5.22	0.158
25 ~ 30	523	7.21	6.70	0.293
30 ~ 35	252	5.09	4.43	0.279
35 ~ 40	88	6.62	5.67	0.605

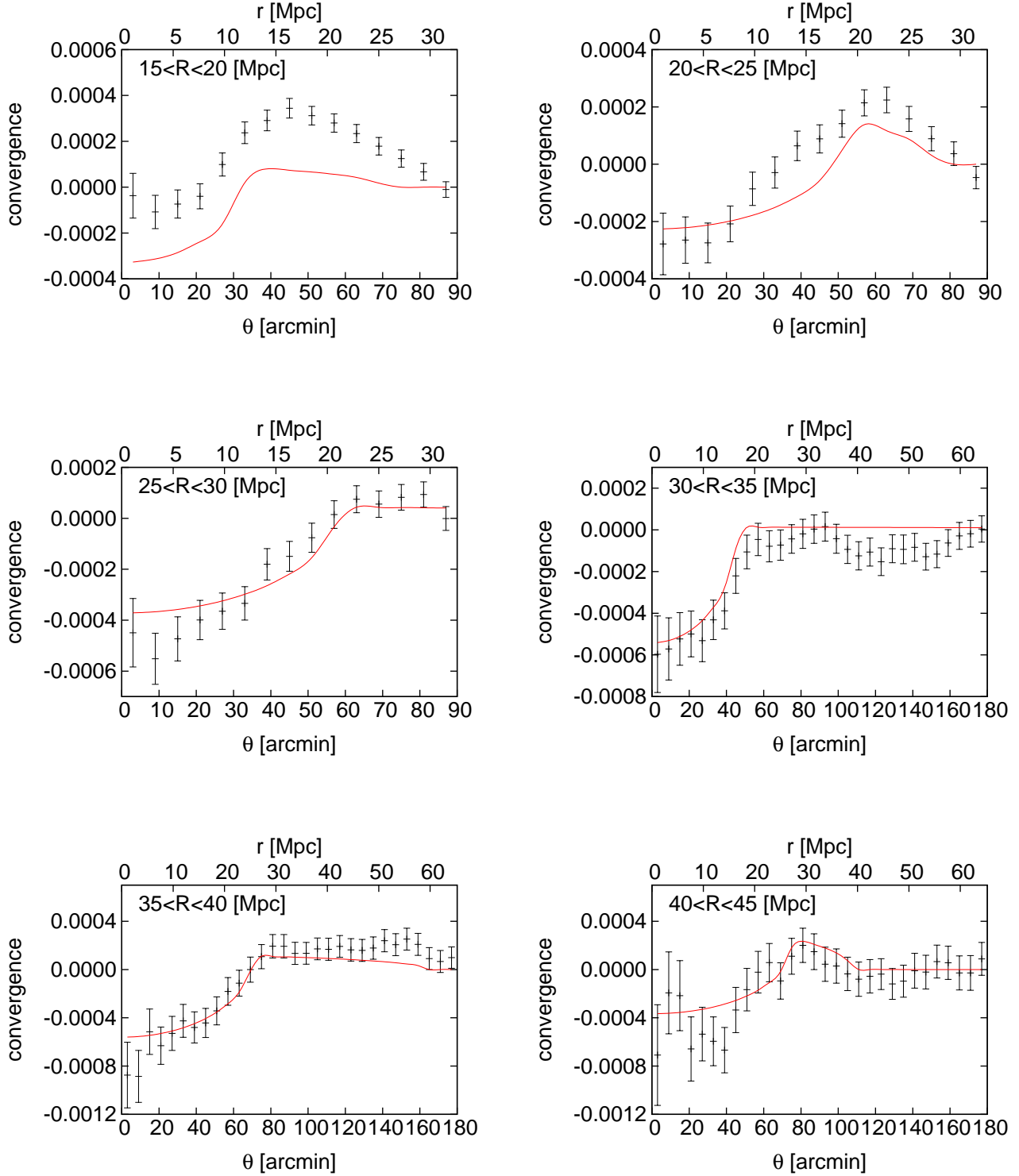


Figure 4. Stacked convergence profiles estimated from simulation (points with errors), the best-fit double top-hat model (solid line), assuming the survey area of 5000 deg^2 , the bin size $\Delta\theta = 6 \text{ arcmin}$ and lens redshift $z_l = 0.5$. Stacking analysis is carried out in each radius derived from the void finder; $15 \leq R \leq 20 \text{ Mpc}$ (top-left); $20 \leq R \leq 25 \text{ Mpc}$ (top-right); $25 \leq R \leq 30 \text{ Mpc}$ (middle-left); $30 \leq R \leq 35 \text{ Mpc}$ (middle-right); $35 \leq R \leq 40 \text{ Mpc}$ (bottom-left); $40 \leq R \leq 45 \text{ Mpc}$ (bottom-right). Best-fit parameters are summarized in table.2.

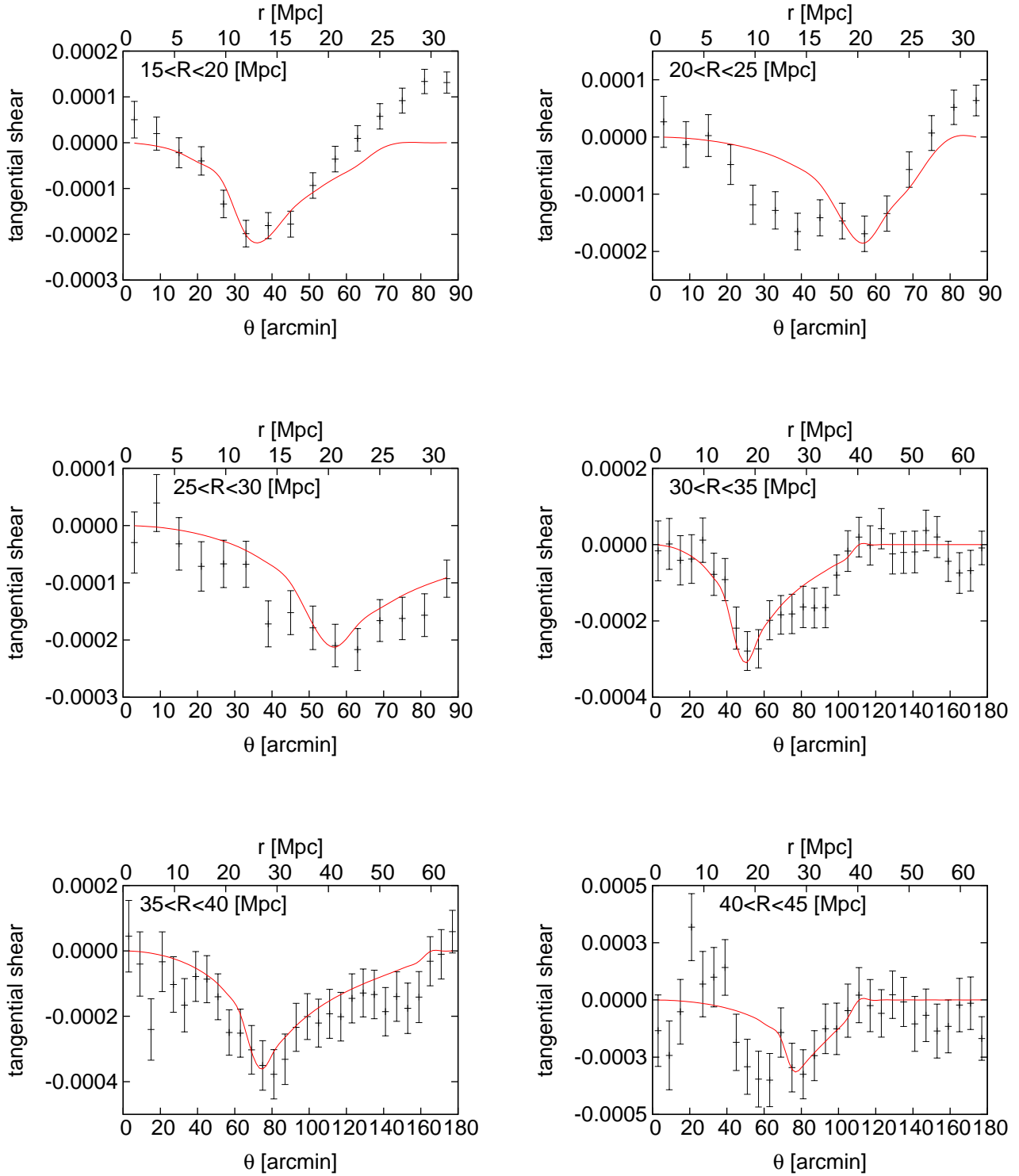


Figure 5. Tangential shear profiles estimated from simulation (points with errors), the best-fit double top-hat model (solid lines) in each radius. Same assumptions in fig.4 are adopted. Stacking analysis are carried out in each radius derived from the void finder; $15 \leq R \leq 20$ Mpc (top-left); $20 \leq R \leq 25$ Mpc (top-right); $25 \leq R \leq 30$ Mpc (middle-left); $30 \leq R \leq 35$ Mpc (middle-right); $35 \leq R \leq 40$ Mpc (bottom-left); $40 \leq R \leq 45$ Mpc (bottom-right). Best-fit parameters are summarized in table.3.

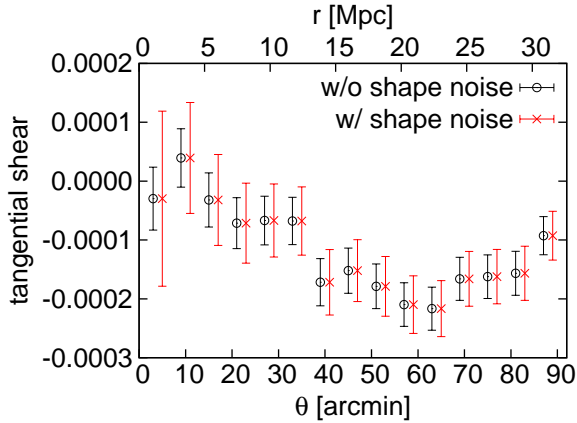


Figure 6. Crosses and circles with errors show the tangential shear profiles for the cases which include the shape noise and not. The stacking analysis are carried out for voids in the radial range $20 \leq R \leq 25$ Mpc. We assume a HSC-type survey, $n_g = 30 \text{ arcmin}^2$, $\sigma_e = 0.4$ and $\text{FOV} = 5000 \text{ deg}^2$.

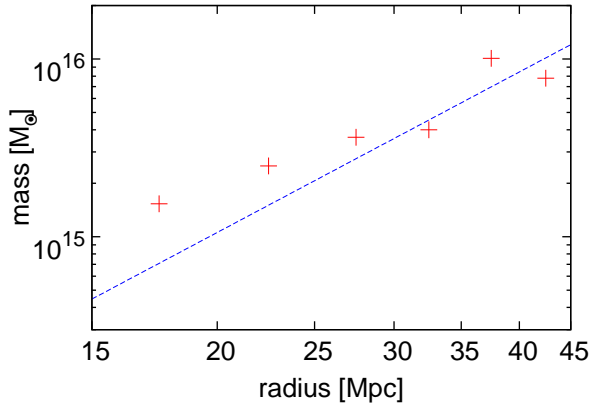


Figure 7. Mass-radius relation. x-axis is radius obtained from void finder. y-axis is mass estimated from our model with tangential shear profiles. Crosses show masses obtained from weak lensing signals and the dashed line plots best-fit curve with eq.34.

where A_0 is constant and we treat it as a free parameter. Fig.7 shows the relationship obtained from the simulation results along with the best-fit model which is determined by the least-square method with A_0 being

$$A_0 = 1.32 \times 10^{11}. \quad (35)$$

Using eq.34, we transform the radius interval to the mass interval, and finally get the void mass function presented in Fig 8.

The best fit modified PS void function is obtained by fitting the simulation result with the analytical function, eq.22 where δ_v is treated as a free parameter. We found the best fit model with $\delta_v = -0.35$. The mass function from the simulation and the best-fit curve of the modified PS model are shown in figure.8. For checking the consistency, we also conduct same procedure using the results from the convergence profile, finding the best-fit linear density of $\delta_v = -0.5$. We note that the parameter δ_v estimated from our model differs from the value predicted from the spherical collapse model $\delta_v = -2.81$ (Sheth & van de Weygaert 2004). There are sev-

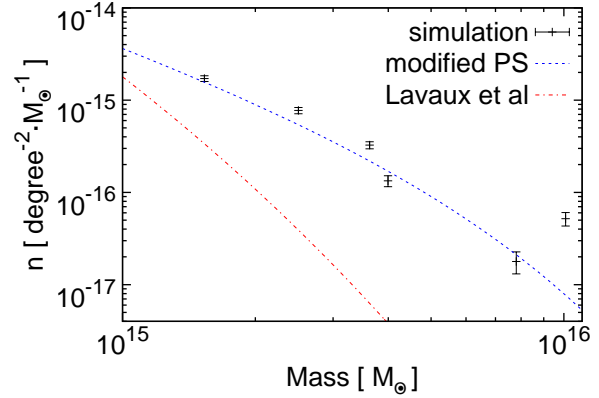


Figure 8. Mass function of voids in simulation and the modified PS theory. Points with errors show the mass function of voids derived from the simulation. Masses are estimated from tangential shear profiles. The number count of voids in the redshift range $0.4 \leq z \leq 0.6$ are used. Error bar shows 1σ of the number count with 200 realizations. The dashed line shows the best-fit curve in the modified PS theory with the linear density fluctuation of $\delta_v = -0.35$. For comparison, we also show the mass function estimated in Lavaux & Wandelt (2012).

eral possible reasons for this, including asphericity of voids and different definition of voids in our study from the spherical collapse model. To explore the origin of the discrepancy is beyond the scope of this paper, and we leave it as future work.

In addition, we also compare the mass function from our simulation with one by Lavaux & Wandelt (2012) in figure.8. Our mass function is higher than that estimated in Lavaux & Wandelt (2012). The reason of this discrepancy is unclear. A possible reason is the difference of void finding algorithms adopted in two studies as statistical properties of voids depend strongly on the definition of the void. The other possibility is the error of mass estimation. The different method to estimate the void mass may account for discrepancy. We leave further investigation on this discrepancy for future work.

7 CONCLUSION

In this paper, we have examined a feasibility of detecting voids with stacked weak lensing. We select voids with a void finder from halo catalogue made from a large set of N -body simulations. We have stacked convergence and tangential shear data from the full ray-tracing simulations to obtain their averaged radial profile (black in fig.4 and fig.5). From our stacking analysis, we have seen both structures of void and ridge outside the void.

To fit the stacked lensing profiles obtained from the simulation, we have considered a simple void model called double top-hat model. Our model fits both profiles of convergence and tangential shear in the simulation very well (fig.4 and fig.5). Estimated total void masses from this model were $M = 10^{14} \sim 10^{16} M_\odot$, which were a few times larger than masses derived from direct integration of the convergence profile at $\kappa(\theta) < 0$. We have confirmed that the dense ridges outside voids affect profiles of weak lensing signals and the

mass estimation of voids. This suggests that we have to properly take account of this effect for interpreting stacked weak lensing signals around voids. The radius of the underdense region derived from model fitting is smaller than the radius derived from the void finder, presumably because the halo catalogue used for finding voids does not directly trace true dark matter distributions.

We also derive the void mass function from simulation results, and compared with the analytical mass function by the modified PS model. We found that the modified PS model with the threshold linear density (but we treat it as a free fitting parameter) can reproduce the simulation result. In addition, we have estimated total S/N to find that stacked lensing signals from voids can be detected at significant level ($S/N \geq 5$) for the 5000 deg^2 area, even if the error coming from the shape noise is added. The shape noise error becomes a dominant component only at the small scale and therefore does not significantly degrade the total S/N.

Our work has demonstrated the observability of voids with the stacked weak lensing method armed with a galaxy (or any tracer of the dark matter distribution) redshift catalogues. In this work, the average number density of halos is $200 / \text{deg}^2 / \Delta z$ for $\Delta z = 0.1$ in the redshift range $0.4 < z < 0.5$. In the SDSS-III Baryon Oscillation Spectroscopic Survey (BOSS) (Dawson et al. 2012), the average number density of luminous red galaxies (LRG) is about $50 / \text{deg}^2 / \Delta z$ for $\Delta z = 0.1$ in the same redshift range. The minimum void size we can identify is mainly determined by the average distance between galaxies. In the simulation, it is about 6.86 Mpc. In BOSS, it is about 10.9 Mpc, which is thus about a factor of two larger than the average distance used in this work. Therefore, it may be possible to find voids from the BOSS data which have large radii, say > 20 Mpc, and to apply the technique described in this paper using weak lensing measurements from e.g., HSC survey. This methodology can also be applied to next generation surveys such as Euclid (Laureijs et al. 2011), Dark Energy Survey (DES) (The Dark Energy Survey Collaboration 2005) and Large Synoptic Survey Telescope (LSST) (LSST Science Collaboration et al. 2009).

The results presented in this paper can be used to estimate the detectability of stacked lensing signal in the HSC survey in combination with the BOSS data. In the discussion above, we assumed that the number density of galaxies is $n_g = 30 \text{ arcmin}^{-2}$ and the source redshift is $z_s = 1$. For the actual HSC survey, however, we can use about 80% galaxies that are located behind $z_1 > 0.6$ the voids we consider, which decreases the number density to $n_g = 24 \text{ arcmin}^{-2}$. On the other hand, we assume a conservative error on the shape of each source galaxy, $\sigma_\epsilon = 0.4$, and as a result the shot noise considered here is close to realistic estimates of the shot noise for the HSC survey (see, e.g. Oguri & Takada 2011). In this case we can simply scale S/N by the survey area. The survey area of the HSC survey is about 1400 deg^2 , indicating that the total S/N is degraded by a factor of $\sqrt{1400/5000} \sim 0.53$. Thus we expect the S/N from voids in the HSC survey is $S/N \geq 3$ for each void group classified by the void radius. Therefore it is possible to detect lensing signals from voids in the HSC survey, particularly if we combine results for several void radius bins.

When we were writing this paper, we came across a paper by Krause et al. (2012) which also studied stacked weak

lensing signals around voids. The main difference of their paper from our analysis is that Krause et al. (2012) assumed analytic mass profiles to estimate S/N, while in this paper we present realistic stacked lensing profiles and the error covariance with ray-tracing of N -body simulations. In addition, Krause et al. (2012) considered voids with smaller radii of $\leq 15h^{-1}\text{Mpc}$ for which our void finder does not work well. Nevertheless, by extrapolating both the results we argue that they are broadly consistent with each other. We also confirmed that the density profile assumed in Krause et al. (2012), which originated from the density profile used in Lavaux & Wandelt (2012), also fits the stacked lensing profiles in our simulation well and produces similar void mass estimates.

ACKNOWLEDGMENTS

We thank an anonymous referee for useful comments. We would like to thank Masanori Sato for providing the raytracing data and Yosuke Utsumi, Tsz Yan Lam, Masahiro Takada for useful discussions and comments. We also thank Caroline Foster for making the code VoidFinder freely available. Numerical computations in the paper were in part carried out on the general-purpose PC farm at Center for Computational Astrophysics, CfCA, of National Astronomical Observatory of Japan. This work was supported in part by the FIRST programme eSubaru Measurements of Images and Redshifts (SuMIRe)f, World Premier International Research Center Initiative (WPI Initiative), MEXT, Japan, and Grant-in-Aid for Scientific Research from the JSPS (23740161), and in part by Grant-in-Aid for Scientific Research from the JSPS Promotion of Science (23540324, 23740161)

REFERENCES

- Amendola L., Frieman J. A., Waga I., 1999, MNRAS, 309, 465
- Bardeen J. M. et al., 1986, ApJ, 304, 15
- Bartelmann M., Schneider P., 2001, Physical Rep., 340, 291
- Broadhurst T. et al., 2005, ApJ, 619, L143
- Clowe D. et al., 2000, ApJ, 539, 540
- Colberg J. M. et al., 2008, MNRAS, 387, 933
- Dawson K. S. et al., 2012, ArXiv e-prints: 1208.0022
- Fahlman G. et al., 1994, ApJ, 437, 56
- Fillmore J. A., Goldreich P., 1984, ApJ, 281, 9
- Foster C., Nelson L. A., 2009, ApJ, 699, 1252
- Furlanetto S. R., Piran T., 2006, MNRAS, 366, 467
- Hamana T., Mellier Y., 2001, MNRAS, 327, 169
- Hoyle F. et al., 2005, ApJ, 620, 618
- Hoyle F., Vogeley M. S., 2004, ApJ, 607, 751
- Jain B., Van Waerbeke L., 2000, ApJ, 530, L1
- Jones D. H. et al., 2004, MNRAS, 355, 747
- Kamionkowski M., Verde L., Jimenez R., 2009, JCAP, 1, 10
- Kirshner R. P. et al., 1981, ApJ, 248, L57
- Klypin A. et al., 1999, ApJ, 522, 82
- Krause E. et al., 2012, ArXiv e-prints: 1210.2446
- Laureijs R. et al., 2011, Arxiv
- Lavaux G., Wandelt B. D., 2012, ApJ, 754, 109
- Lee J., Park D., 2009, ApJ, 696, L10
- Li B., Zhao G.-B., Koyama K., 2012, MNRAS, 421, 3481

- LSST Science Collaboration et al., 2009, ArXiv e-prints: 0912.0201
Mandelbaum R. et al., 2006, MNRAS, 372, 758
Miyazaki S. et al., 2002, ApJ, 580, L97
Miyazaki S. et al., 2006, in SPIE, Vol. 6269, Society of Photo-Optical Instrumentation Engineers (SPIE) Conference Series
Moffat J. W., 2006, JCAP, 5, 1
Oguri M. et al., 2012, MNRAS, 420, 3213
Oguri M., Takada M., 2011, Phys. Rev. D, 83, 023008
Okabe N. et al., 2010, PASJ, 62, 811
Pan D. C. et al., 2012, MNRAS, 421, 926
Park D., Lee J., 2007, Phys. Rev. Let., 98, 081301
Peebles P., 1980, The large-scale structure of the universe
Prada F. et al., 2012, MNRAS, 423, 3018
Press W. H., Schechter P., 1974, ApJ, 187, 425
Roza E. et al., 2010, ApJ, 708, 645
Ryden B. S., Turner E. L., 1984, ApJ, 287, L59
Sato M. et al., 2009, ApJ, 701, 945
Sheth R. K., van de Weygaert R., 2004, MNRAS, 350, 517
Spergel D. N. et al., 2007, ApJS, 170, 377
Springel V., 2005, MNRAS, 364, 1105
Squires G. et al., 1996, ApJ, 469, 73
Squires G. et al., 1997, ApJ, 482, 648
Strauss M. A. et al., 1992, ApJ, 385, 421
Suto Y., Sato K., Sato H., 1984, Progress of Theoretical Physics, 71, 938
Takada M., 2006, Phys. Rev. D, 74, 043505
Tavasoli S., Vasei K., Mohayaee R., 2012, ArXiv e-prints: 1210.2432
The Dark Energy Survey Collaboration, 2005, ArXiv Astrophysics e-prints: 0510346
Umetsu K. et al., 2011, ApJ, 738, 41
Van Waerbeke L. et al., 2000, A&A, 358, 30